Journal of the Optical Society of America B
OPTICAL PHYSICS

Advanced regime of the noncollinear two-phonon acousto-optical interaction governed by elastic waves of finite amplitude and optical spectrum analysis

ALEXANDRE S. SHCHERBAKOV AND ADAN OMAR ARELLANES*

National Institute for Astrophysics, Optics & Electronics (INAOE), Puebla 72000, Mexico
**Corresponding author: arellaneso@inaoep.mx*

Received 31 March 2015; revised 20 July 2015; accepted 21 July 2015; posted 22 July 2015 (Doc. ID 237104); published 18 August 2015

Principally new features of square-law nonlinearity specific to the noncollinear two-phonon acousto-optical interaction (AOI) governed by elastic waves of finite amplitude in birefringent crystals are revealed and studied. An additional degree of freedom represented by the dispersive birefringence factor, which can be distinguished within this nonlinear phenomenon, is found and characterized. This physical degree of freedom gives us a one-of-a-kind opportunity to apply the two-phonon AOI in practice for the first time. The needed theoretical analysis is developed, and proof-of-principle experiments performed with a specially designed unique wide-aperture acousto-optical cell (AOC) made of the calomel (α-Hg_2Cl_2) single crystal, are presented. The results of experiments with this AOC confirm the elaborated theory with numerical estimations and support the proposed application to optical spectrum analysis with the doubled resolution.

OCIS codes: (190.4410) Nonlinear optics, parametric processes; (190.4223) Nonlinear wave mixing; (230.1040) Acousto-optical devices; (300.6320) Spectroscopy, high-resolution.

http://dx.doi.org/10.1364/JOSAB.32.001930

1. INTRODUCTION

Application of the noncollinear acousto-optical interaction (AOI) to optical spectrum analysis has given rise to the noncollinear acousto-optical filters (AOFs) that have been in constant improvement since their appearance in the late 1960s. Unlike the collinear AOFs, which are very restricted to a spectrum of available crystalline materials where the collinear AOI exists, the noncollinear AOFs can work within several optically anisotropic materials. From the beginning, the most desirable material for designing the noncollinear AOFs was tellurium dioxide (TeO_2). This crystal is characterized by extremely low acoustic velocity associated with the slow shear elastic mode passing along the [110]-axis. This fact, together with moderate refractive indexes and a photo-elastic constant, produces a very high acousto-optical figure of merit M_2 [1]. In spite of rather large acoustic losses, which usually accompany slow elastic modes in crystals, exploiting the TeO_2 crystals makes it possible to achieve up to 100% operating efficiency at quite reasonable acoustic power densities. The spectral resolution of about 20 Å at an optical wavelength of $\lambda = 633$ nm was achieved with an efficiency of 96% and an interaction length of ~50 mm [2]. Together with this, the spectral resolution of ~4 Å at the same wavelength was predicted for that crystal with the optimized design [2]. Today, even commercial TeO_2-based AOFs can achieve a spectral resolution of 3.2 Å at $\lambda = 633$ nm with an efficiency higher than 50% [3]. Recently, studies for imaging purposes have exploited tellurium dioxide for theoretical analysis to compensate for the optical dispersion in a noncollinear filter to obtain better performances using the optical activity inherent in the TeO_2 crystal [4].

In recent years, the potassium dihydrophosphate (KDP) crystal has been investigated as a more profitable material for the noncollinear AOFs. This material is suitable for ultraviolet wavelengths thanks to its wide transmission range. Because of the photo-elastic tensor properties of KDP, similar AOFs have to use the slow shear elastic mode passing along a direction tilted by a few degrees to the [100]-axis, which is associated with a higher effective photo-elastic constant, increasing the figure of merit. The KDP crystal is one of the most progressive materials for noncollinear AOFs in the middle- to near-ultraviolet range. The KDP-based noncollinear AOFs promise significantly better performances than the existing α-quartz-based collinear AOFs that are the most widely used and most appropriate AOFs for the ultraviolet [5]. In particular, the KDP crystal has a figure of merit M_2 that is four times higher than a α-quartz crystal [6]. In past years, it has been

reported that the KDP-based noncollinear AOF has been improved by enhancing the angular aperture of this AOF and achieving a spectral resolution of 2.5 Å at $\lambda = 205$ nm [7].

Together with this, the mercurous chloride or calomel (α-Hg_2Cl_2) crystal is another promising material for acousto-optical devices. This material has tetragonal symmetry, anomalously small acoustic velocity for the slow shear elastic mode passing along the [110]-axis (being almost two times lower than in tellurium dioxide), and large refractive indexes and birefringence; it also promises a really high figure of merit M_2. Initially, the acousto-optic properties of small samples of this material were studied in 1976, and, later, crystals about 50 mm long were investigated [8]. The longitudinal acoustic mode (in several directions) can be exploited as well, but the figure of acousto-optical merit of such a configuration is not as great as for the slow shear mode [9]. Currently, we have designed an innovative acousto-optical cell (AOC) based on this previously underrated material for the frontline of information technology.

The main goal of our investigations is to reveal novel physical details inherent in the nonlinearity of a noncollinear two-phonon AOI controlled by elastic waves of finite amplitude, to investigate the features of this nonlinearity (both theoretically and experimentally) in wide-aperture crystals with moderate linear acoustic attenuation, and to consider an opportunity for parallel optical spectrum analysis with the significantly improved spectral resolution. Studying the local unit-level maxima in the distribution of light scattered into the second order, which appear periodically as the power density of the elastic waves grows, makes it possible to identify a variety of the transfer function profiles peculiar to these maxima in the isolated planes of angular-frequency mismatches. Availability of similar maxima gives us an opportunity to choose the desirable profile for the transfer function at the fixed angle of incidence for the incoming light beam with a wide optical spectrum.

Then, we find that noncollinear two-phonon processes of AOI are nearly 100% efficient at the fixed optical wavelength for various acoustic frequencies, as well as with the fixed acoustic frequency for various optical wavelengths because of the existence of an additional dispersive birefringence factor that can be distinguished within this nonlinear phenomenon. However, the first option with the fixed optical wavelength cannot be used for linear spectrum analysis of radio-wave signals, principally owing to the existence of a strong nonlinear dependence between the incoming electronic signal, i.e., the acoustic waves of finite amplitude in an AOC and the scattered light waves. In contrast, under the same conditions, a dependence of the scattered light waves on the incident light is nevertheless linear within the nonlinear noncollinear two-phonon AOI, which can also double the spectral resolution. Therefore, in view of developing a new approach to parallel spectrum analysis of wide-spectrum optical signals with significantly improved resolution, we choose the second option with the fixed acoustic frequency (see Fig. 1), which gives us an opportunity to propose a pioneer practical application of the noncollinear two-phonon AOI for the first time to the best of our knowledge. Generally, the potential spectral resolution of spectrometers exploiting the noncollinear AOC includes the ordinary birefringence of a crystal as a basic parameter of the chosen material, which determines its possibilities.

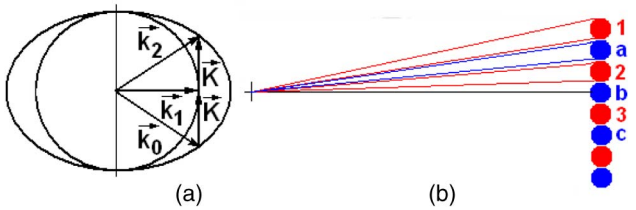

Fig. 1. (a) Noncollinear two-phonon AOI vector diagram and (b) doubling of the spectral resolution. Spots 1,2,3,… are related to one-phonon processes, while additional spots a,b,c,… describe refining the resolution caused by the appearance of a two-phonon interaction.

In applying this new approach, we demonstrate an opportunity to replace the physically limited birefringence of a crystal by the significantly larger birefringence factor, inherent in the noncollinear two-phonon AOI. Moreover, it can be done together with doubling the spectral resolution, which is specific to the noncollinear two-phonon AOI, in principle, as shown in Fig. 1. These possibilities are demonstrated theoretically for the crystals of tetragonal symmetry as examples, and confirmed during the experiments with a specially designed, unique wide-aperture AOC using the calomel (α-Hg_2Cl_2) single crystal and governed by elastic waves of finite amplitude.

2. NONCOLLINEAR TWO-PHONON AOI GOVERNED BY ACOUSTIC WAVES OF FINITE AMPLITUDE

Strong nonlinear behavior of optical components with the Bragg AOI in an anisotropic medium can be achieved easily in usual experiments without any observable influence of the scattering process on the acoustic wave. In this case, the amplitude of the acoustic wave is governed by a homogeneous wave equation in a so-called weak coupling regime [10]. Let us assume that the area of propagation for the acoustic wave, traveling almost perpendicular to the light beams, is bounded by two planes, $x = 0$ and $x = L$, in a uniaxial crystal, taking into account both angular and frequency mismatches in the wave vectors. Usually the Bragg acousto-optical processes include three waves, the incident and scattered light modes, as well as an acoustic mode the processes also incorporate conservation of both the energy and the momentum for each partial act of a one-phonon AOI [11]. However, at certain incident angles of light shining on selected crystal cuts and at a fixed frequency of the acoustic wave, one can observe Bragg scattering of light caused by the participation of two phonons, so that the conservation laws are given by $\nu_1 = \nu_0 + f$, $\vec{k}_1 = \vec{k}_0 + \vec{K}$, $\nu_2 = \nu_0 + 2f$, and $\vec{k}_2 = \vec{k}_0 + 2\vec{K}$ simultaneously (ν_m, $\vec{k}_m$, and f, $\vec{K}$ are the frequencies and wave vectors of the light and acoustic waves, $m = 0, 1, 2$); see Fig. 1(a). Such a four-wave process occurs at the frequency f_0 of the acoustic wave, exactly specific to a two-phonon AOI, which can be determined from [12]

$$f_0 = \lambda^{-1} V b, \tag{1}$$

where $b = \sqrt{|n_0^2 - n_1^2|}$ is a remarkably dispersive birefringence factor; $n_0 \neq n_1$ are the current refractive indexes of a crystal; V is the ultrasound velocity; and λ is the incident light wavelength. The polarization of light in the zero and second orders is orthogonal to the polarization in the first order, whereas the frequencies of the light beams in the first and second orders of scattering are shifted by f_0 and $2f_0$, respectively, with reference to the zero order because of the Doppler frequency shift.

A set of equations for the complex amplitudes $C_m(x)$ of light waves ($m = 0, 1, 2$), appearing because of a quasi-stationary two-phonon Bragg AOI governed by acoustic waves of finite amplitude, is given by [12]

$$\frac{dC_0}{dx} = -\sigma C_1 \exp(-i\eta_0 x), \tag{2a}$$

$$\frac{dC_1}{dx} = \sigma[C_0 \exp(i\eta_0 x) - C_2 \exp(-i\eta_1 x)], \tag{2b}$$

$$\frac{dC_2}{dx} = \sigma C_1 \exp(i\eta_1 x), \tag{2c}$$

where x is the coordinate along light propagation. The combined effect of factors expressing both the acousto-optical material efficiency and the acoustic power is described by $\sigma = \pi(\lambda \cos\theta)^{-1}\sqrt{M_2 P/2}$; θ is the angle of incidence for an external plane light wave, M_2 is the figure of acousto-optical merit, and P is the acoustic power density. A square-law nonlinearity exists that is connected to the products $C_m P^{1/2}$ on the right sides of Eq. (2). The constant angular-frequency mismatches $\eta_m = k_{m,x} - k_{m+1,x}$ are explained in terms of x-components for light wave vectors. We analyze Eq. (2) with the simplest boundary conditions, $|C_0(x=0)|^2 = I$, $C_{1,2}(x=0) = 0$, and exploit the conservation law, $|C_0|^2 + |C_1|^2 + |C_2|^2 = I$, resulting from Eq. (2), where I is the intensity of the incident continuous-wave light beam.

Now, we assume the precise angular alignment of the incident light and expand η_0 and η_1 into a series in terms of powers of only the frequency detuning $|f - f_0|$ for the current acoustic frequency f relative to the frequency $f_0 = \Omega_0/(2\pi)$. In the second order approximation, one can obtain from the diagram of wave vectors that $\eta_0 \approx \pi\lambda n_1^{-1} V^{-2}|f - f_0|^2$ and $\eta_1 \approx \pi\lambda n_0^{-1} V^{-2}(4f_0|f - f_0| + 7|f - f_0|^2)$ [12] with $n_0 < n_1$. Therefore, in the first-order approximation, we may put $\eta_0 \approx 0$ and $\eta \approx \eta_1 \approx 4\pi\lambda n_0^{-1} V^{-2} f_0 |f - f_0|$. After that, one can put $S_{0,1} = C_{0,1}$ and $S_2 = C_2 \exp(-i\eta x)$, and rewrite Eq. (2) as

$$\frac{dS_0}{dx} = -\sigma S_1, \tag{3a}$$

$$\frac{dS_1}{dx} = \sigma(S_0 - S_2), \tag{3b}$$

$$\frac{dS_2}{dx} = \sigma S_1 - i\eta S_2. \tag{3c}$$

Now, the corresponding boundary conditions are

$$S_0(x=0) = 1, \qquad S_{1,2}(x=0) = 0. \tag{4}$$

This set of the combined first-order differential equations can be converted into a triplet of equations of the third order for complex amplitudes S_m, and these equations are independent of each other. In the case of $d\sigma/dx = 0$, these equations reduce to one describing all the light waves:

$$\frac{d^3 S_m}{dx^3} + i\eta \frac{d^2 S_m}{dx^2} + 2\sigma^2 \frac{dS_m}{dx} + i\eta\sigma^2 S_m = 0. \tag{5}$$

The general solution for the complex amplitude S_2 is

$$S_2 = \frac{\sigma^2 \exp(a_1 x)}{(a_1 - a_2)(a_1 - a_3)} - \frac{\sigma^2 \exp(a_2 x)}{(a_1 - a_2)(a_2 - a_3)} + \frac{\sigma^2 \exp(a_3 x)}{a_1 a_2 - a_1 a_3 - a_2 a_3 + a_3^2}, \tag{6}$$

where a_k ($k = 1, 2, 3$) are the roots of the characteristic equation $a^3 + i\eta a^2 + 2\sigma^2 a + i\eta\sigma^2 = 0$ for Eq. (5). This solution leads to a 3-dimensional (3-D) distribution $|C_2|^2 = |S_2(\sigma x, \eta x)|^2$, expressed in terms of two dimensionless parameters, σx and ηx, describing the acoustic power density and the angular-frequency mismatch, respectively; see Fig. 2. This plot demonstrates a specific square-law acousto-optical nonlinearity inherent in the noncollinear two-phonon AOI governed by elastic waves of finite amplitude. Moreover, Fig. 3 exhibits a sequence of unit-level maxima that are often desirable for potential practical applications, particularly to the spectrum analysis of optical signals. The first quartet of maxima is placed

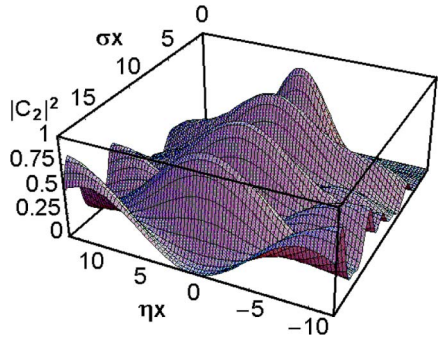

Fig. 2. 3-D-band shape for the noncollinear two-phonon AOI; the axis σx (the dimensionless acoustic power density) reflects nonlinearity of the phenomenon; ηx is the dimensionless angular-frequency mismatch.

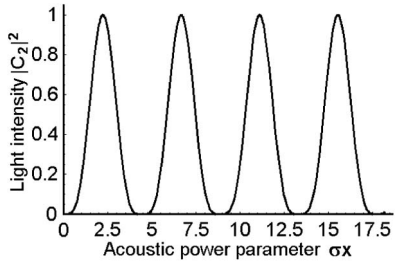

Fig. 3. Maxima of the noncollinear two-phonon AOI reflecting its strong nonlinear behavior along the line $\eta x = 0$.

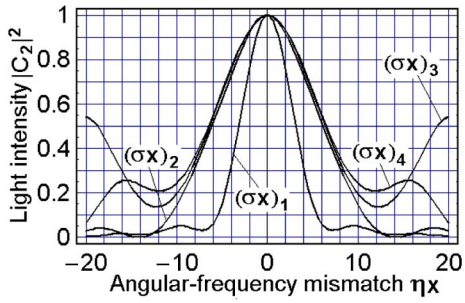

Fig. 4. Intensity mismatch profiles related to first four maxima of the noncollinear two-phonon AOI.

at the points $(\sigma x)_1 \approx 2.22$, $(\sigma x)_2 \approx 6.66$, $(\sigma x)_3 \approx 11.11$, and $(\sigma x)_4 \approx 15.55$. At these points, one can obtain four particular profiles in terms of the dimensionless angular-frequency mismatch ηx; see Fig. 4.

Then, the plots in Fig. 4 also demonstrate an influence of specific acousto-optical square-law nonlinearity and show that the second maximum in Fig. 3 already shows close to the widest bandwidth of a two-phonon AOI at a reasonably high acoustic power parameter $(\sigma x)_2 \approx 6.66$. Consequently, this exact maximum with a two-sided variation of the dimensionless mismatch about $\Delta\eta = (\eta x)_- + (\eta x)_+ \approx 4\pi$ at the half-maximum level can be selected as the most appropriate one for realizing a wide-bandwidth two-phonon AOI. In the case of exact angular alignment, the mismatch η is only achieved by the frequency detuning $|f - f_0|$ so that, as it is seen directly from Eq. (2), $\eta = 2\pi|f - f_0|/V$. With $x = L$, the second profile from Fig. 4 leads to $\Delta\eta \approx 2\eta \approx 4\pi/L$ so that the frequency bandwidth for the second maximum is given by

$$\Delta f = 2|f - f_0| \approx n_0 V^2/(\lambda L f_0). \quad (7)$$

Here, the length L of AOI, the current frequency f_0, and the optical wave length λ have to provide the Bragg regime of AOI.

3. FREQUENCY AND LENGTH OF AN AOC BASED ON THE NONCOLLINEAR TWO-PHONON AOI IN A TETRAGONAL α-Hg_2Cl_2 CRYSTAL

To make our consideration more concrete, an appropriate acousto-optically effective crystalline material will be selected for further analysis. During the selection of a similar appropriate material, a few possibilities of exploiting either longitudinal L or shear S elastic modes passing along various directions were preliminarily estimated. In particular, the subjects of our attention were the modes $L[001]$ and $S[110]$ in rutile (TiO_2), $S[100]$ in lithium niobate ($LiNbO_3$), and $L[100]$ and $S[110]$ in calomel (α-Hg_2Cl_2). These modes allow the noncollinear two-phonon AOI and can be considered as desirable alternatives operating at rather different acoustic frequencies. The analysis has shown that the best option for further experiments, motivated by a very high efficiency of AOI and an acoustic frequency that is not too high, is the calomel single crystal. This crystal belongs to the 4/mmm-tetragonal symmetry group, has a spectral transmission band of $\Delta\lambda = 0.38$–28 μm, and has a material density of $\rho \approx 7.2$ g/cm^3 [13]. It has a pair of dispersive refractive indexes whose main values are $N_O = 1.9634$ and $N_E = 2.6217$ at the wavelength $\lambda = 633$ nm. Then, in particular, this crystal allows at least two pure elastic modes, namely, the slow shear mode with the wave vector $\vec{K}\|[110]$, the displacement vector $\vec{u}\|[1\bar{1}0]$, the phase velocity $V_{SS} \approx 0.347 \times 10^5$ cm/s, and the acoustic wave attenuation factor $\Gamma \approx 230$ dB/(cm GHz^2). There is also the longitudinal mode with $\vec{K}\|\vec{u}\|[100]$, $V_L \approx 1.622 \times 10^5$ cm/s, and $\Gamma \approx 12.5$ dB/(cm GHz^2). It is important to note that both these elastic modes are potentially suitable for an effective noncollinear two-phonon AOI.

Now, we make the new step of studying the nonlinearity of noncollinear two-phonon AOI; see Fig. 5. This step can be represented for the corresponding processes of scattering in terms of two surfaces for the refractive indexes of ordinary (see the internal dark sphere) and extraordinary (see the external faint ellipsoid) light waves for a tetragonal crystal at the fixed optical wavelength λ. (Here, the calomel crystal at $\lambda = 633$ nm is taken as an example with $N_E \geq N_O$.) The sizes of both the sphere and the ellipsoid will be varied depending on λ because of the remarkable dispersion of the crystalline material within a potential optical range. The vertical axis in Fig. 5 is oriented along the optical axis [001] of a crystal, while orientation for a pair of the horizontal axes depends on the chosen elastic modes.

For the calomel crystal, in particular, these axes can be taken as [110] and [1$\bar{1}$0] for the slow shear mode, or as [100] and [010] for the longitudinal mode. Then, in either case, this figure includes a pair of vector diagrams illustrating two opportunities for two-phonon AOI through various angles, which use different acoustic frequencies and birefringence factors b. Two triplets of vectors, going from the geometric center of surfaces, represent the optical wave vectors describing the corresponding orders of AOI, whereas sequential pairs of the acoustic wave vectors reflect two-phonon processes. The upper vector diagram in Fig. 5 corresponds to the smaller birefringence, i.e., to smaller factor b, and the lower acoustic frequency f_0, i.e., to shorter vectors $\vec{K}$, than the lower one shows. The lower vector diagram operates by larger factor b and higher acoustic frequency f_0, i.e., by longer vectors $\vec{K}$. Thus, these plots reflect

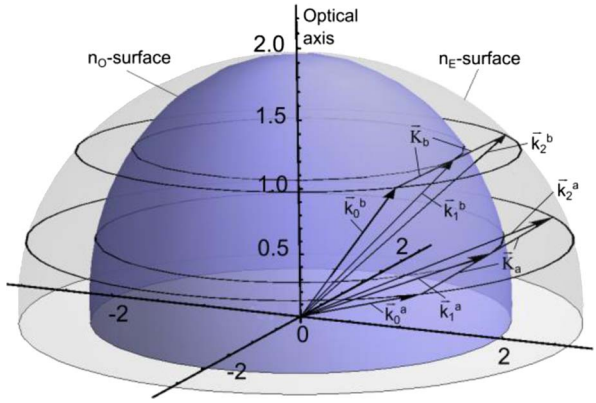

Fig. 5. Two examples of vector diagrams, indexed by "a" and "b," inherent in nonlinear two-phonon AOI with the fixed ratio V/λ. The extraordinary refractive index n_E is described by an external faint ellipsoid, while a darker internal sphere shows the ordinary refractive index $n_O \equiv N_O$. Here, $\vec{k}_m^{a,b}$ and $\vec{K}_{a,b}$ are the wave vectors of light and acoustic waves.

the existence of an additional physical degree of freedom inherent in the nonlinearity of the two-phonon AOI. This degree of freedom permits the fixed frequency f_0 to exert control over various optical wavelengths scattered through different angles. In this case, one has to consider two pairs of surfaces specific to the refractive indexes of ordinary and extraordinary light waves for a tetragonal crystal, and each similar pair of surfaces corresponds to an individual light wavelength. Nevertheless, the corresponding vector diagrams for two different nonlinear processes of two-phonon AOI will include acoustic vectors $\vec{K}$ of the same lengths characterizing the same acoustic frequency f_0.

Calomel is a uniaxial crystal, so that $n_O \equiv N_O$ is the main refractive index for the ordinary state of polarization, while n_E depends on a direction in a crystal and has the form of an ellipsoid. We are interested in rather small tilts from the [001]-axis. Therefore, one can consider the angle $\psi \in [0, \pi/2]$ of a tilt from the [001]-axis. The geometric interpretation yields

$$n_E^2 = \frac{N_E^2 N_O^2 (1 + \tan^2 \psi)}{N_E^2 + N_O^2 \tan^2 \psi} \geq n_O^2 \equiv N_O^2. \quad (8)$$

Substituting Eq. (8) into Eq. (1), one can obtain

$$\psi[\text{rad}] = \arctan\left[\frac{\lambda f_0 N_E}{N_O \sqrt{V^2 (N_E^2 - N_O^2) - \lambda^2 f_0^2}}\right]. \quad (9)$$

Then, within designing an AOC based on a crystal with moderate acoustic losses and under the action of the acoustic wave of finite amplitude, the spectral resolution $\delta\lambda_0$ of a potential dispersive component based on a similar AOC can be estimated as

$$\delta\lambda_0 = \lambda^2/(2bD). \quad (10)$$

This value does not include any parameters of the acoustic wave, and, besides the optical aperture D, depends only on the birefringence factor b specific to a crystal and the incident light wavelength λ. The desirable aperture D in Eq. (10) has to be chosen to satisfy a few requirements depending on a set of various physical factors; the main one is the acoustic attenuation. If an acceptable level of acoustic losses per optical aperture D is B [dB/aperture], one can write that $D = B/(\Gamma f_0^2)$. From these formulas, one can find the denominator in Eq. (10) to be

$$2bD = \frac{2\lambda B}{V\Gamma f_0}. \quad (11)$$

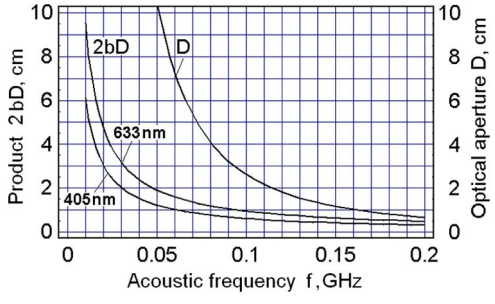

Fig. 6. Product 2 b D and the desirable aperture D, connected with the spectral resolution, for the slow shear elastic mode in the calomel.

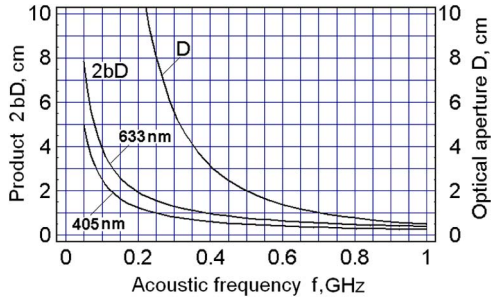

Fig. 7. Product 2 b D and the desirable aperture D, connected with the spectral resolution, for the longitudinal elastic mode in the calomel.

Restricting ourselves to the level $B \equiv 6$ dB/aperture and using the above-mentioned data for the two chosen pure elastic modes in the calomel, one can obtain for $\lambda = 405$ and 633 nm (see the following plots shown in Figs. 6 and 7).

Before we analyze these diagrams further, we motivate the above taken selection of the level $B = 6$ dB for acoustic losses per optical aperture. As such, we attempt to describe shaping the resolvable spot after an AOC in a spectrum analyzer. The normalized distribution $I(u)$ of light intensity of that individual resolvable spot is given by

$$I(u, \alpha_0) = \frac{\sin^2(\pi u) + \sinh^2(\alpha_0/2)}{[1 + (2\pi u/\alpha_0)^2]\sinh^2(\alpha_0/2)}, \quad (12)$$

where $u = wD/\lambda F$; w is the physical spatial coordinate in the focal plane; F is the focal distance of the integrating lens; and $\alpha_0 = \alpha D$ is the acoustic loss factor per aperture. An analysis of Eq. (12) shows that $\alpha_0 \equiv B = 6$ dB/aperture gives the first zero in the distribution $I(u)$ at a level of about –20 dB. Choosing $B = 6$ dB allows us to avoid unnecessarily strong limitations for this stage of studies. Together with this, the main lobe in the distribution $I(u)$ will be almost no wider at $B = 6$ dB/aperture.

4. EFFICIENCY OF THE NONCOLLINEAR TWO-PHONON AOI IN α-Hg_2Cl_2 UNIAXIAL CRYSTAL

Obtaining the figure of acousto-optical merit M_2 inherent in the selected cut of an α-Hg_2Cl_2 crystal first requires finding the effective photo-elastic constant p_{eff}. To do so, keep in mind that each dynamic acoustic grating can be characterized by its symmetric deformation tensor of the second rank $\gamma = (\vec{u} \cdot \vec{q} + \vec{q} \cdot \vec{u})/2$, where $\vec{q} = \vec{K}/|K|$ is the unit vector of the wave normal.

A. Case of the Slow Shear Elastic Mode with $\vec{K} \| [110]$, $\vec{u} \| [1\bar{1}0]$

Because of $\vec{q} = (1, 1, 0)/\sqrt{2}$ and the normalized displacement vector of $\vec{u} = (1, -1, 0)/\sqrt{2}$, the corresponding deformation tensor takes the following dyadic form:

$$\gamma^{(S)} = 0.5\{(\vec{x}_1 \bullet \vec{x}_1) - (\vec{x}_2 \bullet \vec{x}_2)\}. \quad (13)$$

The tensor $\gamma^{(S)}$ of the second rank with the components $\gamma_{kl}^{(S)}$ $(k, l = 1, 2, 3)$ in the basis $(\vec{x}_1, \vec{x}_2, \vec{x}_3)$ can be converted into a six-dimensional (6-D) vector $\tilde{\gamma}^{(S)} = (1, -1, 0, 0, 0, 0)$ [14].

To estimate the efficiency of AOI associated with the above selected slow shear acoustic mode, the photo-elastic tensor p of the fourth rank should be converted into the form of a 6 × 6 matrix with the components $p_{\lambda\mu}$. For α-Hg_2Cl_2 (4/mmm), the matrix representation for the tensor p gives the following nonzero components: $p_{11} = p_{22} = 0.551$, $p_{12} = p_{21} = 0.44$, $p_{13} = p_{23} = 0.256$, $p_{31} = p_{32} = 0.137$, $p_{33} = 0.1$, $p_{44} = p_{55}$—unknown, and $p_{66} = 0.047$ at $\lambda = 633$ nm [15]. Now, one can calculate the matrix product $p\tilde{\gamma}^{(S)} = 0.5(p_{11} - p_{12})(1, -1, 0, 0, 0, 0)$ and convert it back to the form of a standard tensor $(p\gamma^{(S)})$ of the second rank [14]. The effective photo-elastic constant can be written from the scalar form $p_{\text{eff}}^{(S)} = \vec{e}_1(p\gamma^{(S)})\vec{e}_0$, i.e.,

$$p_{\text{eff}}^{(S)} = 0.5(p_{11} - p_{12})\vec{e}_1[(\vec{x}_1 \bullet \vec{x}_1) - (\vec{x}_2 \bullet \vec{x}_2)]\vec{e}_0, \quad (14)$$

where the vectors $\vec{e}_0$ and $\vec{e}_1$ usually describe the polarization states of incident and scattered light beams, respectively. Within the anomalous noncollinear AOI, the eigen polarization vectors $\vec{e}_0$ and $\vec{e}_1$ of the incident and scattered light beams should be orthogonal to each other $\vec{e}_0 \perp \vec{e}_1$, but they both should also be lying in the same plane as the wave vector $\vec{K} \| [110]$.

For the sake of simplicity, in this case, one can take $\vec{e}_0 \| \vec{K}$ and $\vec{e}_1 \| \vec{u}$, i.e., $\vec{e}_0 = (1, 1, 0)/\sqrt{2}$ and $\vec{e}_1 = (1, -1, 0)/\sqrt{2}$. Then, one can obtain $(p\gamma^{(S)}) \cdot \vec{e}_0 = 2^{3/2}(p_{11} - p_{12})(1, -1, 0)$ and find

$$p_{\text{eff}}^{(S)} = \vec{e}_1(p\gamma^{(S)})\vec{e}_0 = 0.5(p_{11} - p_{12}) \approx 0.055. \quad (15)$$

The corresponding figure of acousto-optical merit M_2 also depends on the material density $\rho = 7.2$ g/cm^3 and a pair of rather dispersive refractive indexes. Using, for instance, $n_O = 1.9634$ and $n_E = 2.6217$ at $\lambda = 633$ nm, one can find $M_2^{(S)} = n_O^3 n_E^3 (p_{\text{eff max}}^{(S)})^2/(\rho V_{SS}^3) \approx 1371 \times 10^{-18}$ s^3/g. This value demonstrates that the anomalous regime of AOI governed by the pure slow shear acoustic mode in the calomel single crystal is very efficient and is able to provide an effective two-phonon AOI.

B. Case of the Longitudinal Elastic Mode with $\vec{K} \| \vec{u} \| [100]$

Exploiting the above described procedure with $\vec{q} = \vec{u} = (1, 0, 0)$, one can obtain a 6-D vector $\tilde{\gamma}^{(L)} = (1, 0, 0, 0, 0, 0)$ and then find $p\tilde{\gamma}^{(L)} = (p_{11}, p_{21}, p_{31}, 0, 0, 0)$ [14] with $p_{11} = 0.551$, $p_{21} = 0.44$, and $p_{31} = 0.137$. Consequently, the effective photo-elastic constant can be expressed as $p_{\text{eff}}^{(L)} = \vec{e}_1(p\gamma^{(L)})\vec{e}_0$, i.e.,

$$p_{\text{eff}}^{(L)} = \vec{e}_1\{p_{11}(\vec{x}_1 \bullet \vec{x}_1) + p_{21}(\vec{x}_2 \bullet \vec{x}_2) + p_{31}(\vec{x}_3 \bullet \vec{x}_3)\}\vec{e}_0, \quad (16)$$

where, as before, the vectors $\vec{e}_0$ and $\vec{e}_1$ describe the polarization states of incident and scattered light beams, respectively. Then they should be orthogonal to one another $\vec{e}_0 \perp \vec{e}_1$ and lie in the plane that includes the wave vector $\vec{K} \| [100]$. Because of $p_{21} > p_{31}$, the most attractive option appears via choosing $\vec{e}_{0,1} \in (010)$ with $\vec{e}_0 = (\cos\alpha, \sin\alpha, 0)$ and $\vec{e}_1 = (-\sin\alpha, 0, \cos\alpha)$, where α is an angle between vectors $\vec{e}_0$ and $\vec{K} \| [100]$. Such a choice leads to

$$p_{\text{eff}}^{(L)} = \vec{e}_1(p\gamma^{(L)})\vec{e}_0 = -0.5(p_{11} - p_{13})\sin(2\alpha). \quad (17)$$

With $\alpha = \pi/4$, one will have $p_{\text{eff max}}^{(L)} = -(p_{11} - p_{13})/2 \approx -0.207$. Consequently, using the above-mentioned data, one can estimate $M_2^{(L)} = n_O^3 n_E^3 (p_{\text{eff max}}^{(L)})^2/(\rho V_L^3) \approx 190.2 \times 10^{-18}$ s^3/g. These calculations show that the anomalous regime of AOI controlled by the pure longitudinal elastic mode is also efficient and can be used to realize a sufficiently effective noncollinear two-phonon AOI in the calomel as well.

5. THEORETICAL ESTIMATIONS OF A DISPERSIVE COMPONENT BASED ON THE CALOMEL-MADE CRYSTALLINE AOC

Now, using the above-obtained data, the plots in Figs. 6 and 7 allow us to estimate potential performances for a dispersive component based on the calomel-made crystalline AOC with the optical aperture $D = 10$ cm.

A. Realizing the Bragg Regime of a Two-Phonon AOI

The length L of Bragg AOI in a crystal is restricted by the following inequality for the Klein–Cook parameter: $Q = 2\pi\lambda L f_0^2/(n_0 V^2) \gg 1$ [16]. In the calomel, for the slow shear mode passing along the [110]-axis with $V_{SS} = 0.347 \times 10^5$ cm/s, $f_0^{(S)} = \sqrt{B/(D\Gamma_S)} \approx 51.075$ MHz, and $n_0 = 2.0826$ at $\lambda = 405$ nm, one finds that $L_{\text{min}}^{(S)} \gg 0.0038Q$ cm. Taking $Q = 4\pi$, one yields $L_{\text{min}}^{(S)} \geq 0.05$ cm and can take $L_{\text{min}}^{(S)} \approx 0.2$ cm with a safety margin. For the pure longitudinal mode passing along the [100]-axis with $V_L = 1.622 \times 10^5$ cm/s, $f_0^{(L)} = \sqrt{B/(D\Gamma_L)} \approx 219.1$ MHz, and $n_0 = 2.0826$ at $\lambda = 405$ nm, one can find $L_{\text{min}}^{(L)} \gg 0.0045Q$ cm, so that the minimal interaction length can be so small that one can use the previous estimation of $L_{\text{min}} \approx 0.2$ cm.

B. Effect of the Acoustic Beam Divergence

The angular divergence of the acoustic beam can be considered via estimating the length X of the Fresnel acoustic zone when the unknown radiating acoustic aperture is equal to R. These values are connected with one another as $X = R^2 f/(2V)$ [17]. If it is granted that the acoustic beam belongs to the Fresnel acoustic zone and $X = 10$ cm, one finds for α-Hg_2Cl_2 that $R \approx \sqrt{2V_S X/f_S} = \sqrt{2V_L X/f_L} \approx 0.12$ cm. Thus, with $R \geq 0.15$ cm, which lies in the frames of the above agreed upon value and is a rather typical value in practice, one can say that potential angular divergence of the acoustic beam is small enough to be omitted, so that the plane-wave approximation is rather close to the reality.

C. General Estimations for the Calomel-Made AOC

At first, let us perform theoretical estimations for the calomel-made AOC with $D = 10$ cm and $L_{\text{min}} \approx 0.2$ cm. The summary of similar estimations is presented in Tables 1 and 2. One can see from these tables that the highest spectral resolution and the largest number of resolvable spots within the widest spectral range can be achieved in the calomel with the exploitation of the pure slow shear elastic mode.

To compare these results with the collinear AOF based on a long aperture $L = 10$ cm lithium niobate ($LiNbO_3$) crystal,

Table 1. Theoretical Estimations[a]

Wavelength λ, nm	n_O	Elastic Mode	V, 10^5 cm/s	Γ, dB/(cm GHz^2)	δf, kHz	f_0, MHz	$\delta\lambda$, Å	2 b D, cm
405	2.0826	S[110]	0.347	230	1.735	51.08	0.1376	1.192
		L[100]	1.622	12.5	8.11	219.1	0.150	1.0935
633	1.9634	S[110]	0.347	230	1.735	51.08	0.2151	1.863
		L[100]	1.622	12.5	8.11	219.1	0.234	1.7094

[a]Here, $\delta f = V/2D$ and $\delta\lambda = \delta f\,\lambda/f_0$ are frequency and spectral resolutions, $f_0 = \sqrt{B/(D\Gamma)}$ is the central acoustic frequency, and the product 2 b $D = \lambda^2/\delta\lambda$ includes the birefringence factor.

Table 2. Practical Estimations[a]

Wavelength λ, nm	n_O	Elastic Mode	Δf, MHz	$\Delta\lambda$, Å	N, spots
405	2.0826	S[110]	6.07	482	3500
		L[100]	30.877	571	3807
633	1.9634	S[110]	3.66	454	2110
		L[100]	18.630	538	2300

[a]Here, $\Delta f = 2|f - f_0| \approx n_0 V^2/(\lambda \mathrm{L} f_0)$ and $\Delta\lambda = \Delta f\lambda/f_0$ are frequency and spectral bandwidths, while $N = \Delta f/\delta f = \Delta\lambda/\delta\lambda$ is the number of resolvable spots.

for example, at $\lambda = 633$ nm, we choose a wavelength that has $N_O = 2.28646$, $N_E \approx 2.20222$, and $|\Delta n| \approx 0.08424$ at $\lambda = 633$ nm to avoid well-known possible problems with the effect of photorefraction in this crystal. Then, one has to take into account that the collinear AOI does not exhibit the above discussed degree of freedom given by Eq. (1). As a result, it is able to give exactly one resolvable spot, i.e., to provide only sequential optical spectrum analysis. Within the collinear interaction, the optical wavelength λ and the corresponding acoustic wave frequency are unambiguously connected. Therefore, for $\lambda = 633$ nm, it requires $f = |\Delta n|V/\lambda \approx 0.8743$ GHz for a pure longitudinal elastic mode with $\vec{K}\|[100]$ in the lithium niobate crystal that has $V_L \approx 6.57 \times 10^5$ cm/s and $\Gamma \approx 0.15$ dB/(cm GHz^2) [1]. This is why one can find that the optical aperture, or, equivalently in the collinear case, the length of the AOI is $L = B/(\Gamma f_0^2) \approx 40$ cm with a $B = 6$ dB/aperture. Of course, such a crystal length is unachievable in practice because of technological limitations, and one has to take $L \le 10$ cm. In this case, one can estimate that $|\Delta n|L \approx 0.842$ cm and $\delta\lambda^{(L)} = \lambda^2/(|\Delta n|L) \approx 0.473$ Å. This result can be marked like an individual level (or a point) on both the diagrams in Figs. 6 and 7. Interestingly, this comparison shows that developing a new approach to optical spectrum analysis is possible. Thus, we propose a parallel algorithm of signal processing with an appreciably improved spectral resolution.

6. PROOF-OF-PRINCIPLE EXPERIMENTAL DATA

A. Experiment Arrangement

First, one can estimate the potential contributions of the acoustic losses for the chosen slow shear elastic mode passing along the [110]-axis whose displacement vector is oriented along the [1$\bar{1}$0]-axis. The coefficient of linear attenuation is $\Gamma \approx 230$ dB/(cm GHz^2) in a calomel single crystal [15]. The factor α[cm^{-1}] of the amplitude acoustic losses is α[cm^{-1}] $= 0.1152\,\Gamma$[dB/(cm GHz^2)]f^2[GHz]. The carrier frequency, specific to the noncollinear two-phonon AOI in calomel, can be calculated as $f_0 \approx 71$ MHz at the above chosen light wavelength 405 nm. Consequently, one can estimate the amplitude factors for acoustic losses by $\gamma = \Gamma f_0^2 \approx 1.16$ dB/cm and $\alpha = 0.134$ cm^{-1}.

The angular divergence of the acoustic beam in the calomel noncollinear AOC at the frequency $f_0 \approx 71$ MHz can be estimated as well. A reliable spatial size of the initial acoustic beam aperture that we will consider is close to $L \approx 0.2$ cm. With $V_{SS} = 0.347 \times 10^5$ cm/s, one can calculate the corresponding acoustic wavelength $\Lambda = V/f_0 = 0.489 \times 10^{-3}$ cm and the angle of acoustic beam divergence $\phi = \Lambda/L \approx 0.244 \times 10^{-2}$ rad $\approx 0.14°$ to conclude that the angular divergence of the acoustic beam can be omitted.

Now, we are ready to perform the few important numerical estimations inherent in the noncollinear interaction at the light wavelength of $\lambda = 405$ nm in the calomel crystalline cell with $M_2 \approx 2546 \times 10^{-18}$ s^3/g and $L = 0.2$ cm. The periodicity of the unit-level AOI maxima (see Fig. 3) gives us an opportunity to choose the second maximum with one of the widest band shapes at $(\sigma x)_2 \approx 6.667$, so that putting $x \equiv L$, one can find $\sigma_2 \approx 33.3$ cm^{-1}. Using the standard determination for σ [18] with $\cos\theta \approx 1$, one can write

$$P \approx \frac{2\lambda^2\sigma^2}{\pi^2 M_2}. \tag{18}$$

Consequently, at $\lambda = 405$ nm, Eq. (18) gives $P_2 \approx 145$ mW/mm^2 for the second maximum. Additionally, one has to take into account the losses needed for converting the electronic signal into an acoustic one, which are, in practice, close to 2–3 dB as the case requires. Usually we have to restrict ourselves to a maximum level $P \le 0.5$ W/mm^2 of acoustic power density. This requires the absolute acoustic power magnitude of about 2 W and the acoustic beam cross section of about 4 mm^2 in the AOC under consideration. The produced estimations demonstrate that the above obtained level for P_2 lies in the ranges of accessible value, while similar parameters P_2 and σ_2 for the second unit-level AOI maximum are beyond these frames. One can see from Fig. 3 that reaching the next maximum needs a much higher acoustic power density in comparison with the second one. This looks rather conjectural from the viewpoint of requirements for the electric strength inherent in the available piezoelectric transducer. After that, preexperimental estimations for the calomel-made AOC with $D = 5.2$ cm and $L_{\min} \approx 0.2$ cm can be summarized in Table 3. These estimations exploit the pure slow shear elastic mode with the acoustic velocity $V_{SS} = 0.347 \times 10^5$ cm/s in the scheme

Table 3. Pre-experimental Estimations[a]

λ, nm	n_O	n_E	d_S, μm	δf, kHz	M_2, s^3/g	$\delta\lambda$, Å	2 b D, cm	P_2, mW/mm^2
405	2.0826	3.0379	6.620	3.337	2.5 10(-15)	0.190	0.862	145
633	1.9634	2.6217	10.347	3.337	1.4 10(-15)	0.368	1.347	657

[a]Here, $d_S = \lambda F/D$ is an ideal spot size in the approximation of geometric frequency, M_2 is the figure of acousto-optical merit, and P_2 is the acoustic power density needed for the second maxima.

of the standard acousto-optical spectrum analyzer with the integrating lens of the focal distance $F = 85$ cm.

The design of the calomel crystalline AOC under consideration, operating in the regime of the noncollinear two-phonon AOI, is presented in detail in Fig. 8. The piezoelectric transducer represented by a thin plate made of the 163° Y-cut $LiNbO_3$ single crystal was placed on the (110) crystallographic plane of the calomel crystal and provided the slow shear mode acoustic beam cross section of about 4 mm^2 at the length $L = 0.2$ cm of AOI in the calomel.

At $\lambda = 405$ nm and the above estimated acoustic wavelength of $\Lambda = 0.489 \times 10^{-3}$ cm, one can find the Bragg angle θ_0 [see Fig. 8(a)] needed for the noncollinear two-phonon AOI as $\theta_0 \approx 0.0414$ rad $\approx 2.37°$. Together with this, the tilt angle ψ needed for $D = 5.2$ cm and $f_0 \approx 71$ MHz [see Fig. 8(b)] can be estimated from Eq. (9) by the value $\psi \approx 0.0546$ rad $\approx 3.13°$ with $\lambda = 405$ nm, $V_{SS} = 0.347 \times 10^5$ cm/s, $N_O = 2.0826$, and $N_E = 3.03794$ in the calomel. Our proof-of-principle experiments were performed with the specially designed wide-aperture AOC based on the unique calomel single crystal. This pioneer AOC works at optical wavelength $\lambda = 405$ nm, which combines the convenience of operating in just the visible range with the best expected optical performances inherent in this AOC with violet light from the single frequency solid-state laser CL-405-050–S (CrystaLaser). Theoretically (see Section 5), the calomel-based AOC could be governed by the radio-wave signals whose best acoustic

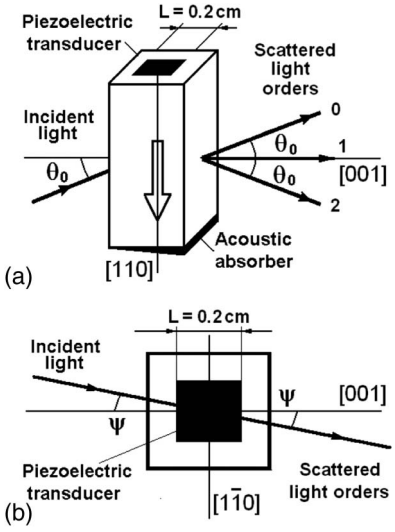

Fig. 8. Design of the calomel AOC: (a) depicts the general view with the Bragg angles of incidence and scattering in three orders, while (b) shows the top view with the needed tilt angle ψ.

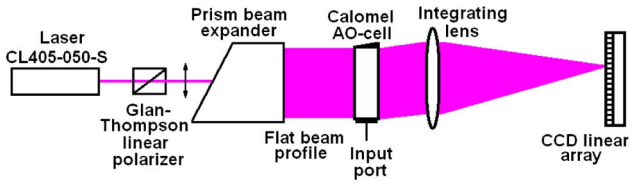

Fig. 9. Layout of the optical scheme; only the second order of a two-phonon AOI is shown.

performances were expected at the central frequency of about 71 MHz, frequency bandwidth of $\Delta f \approx 4.36$ MHz, and frequency resolution of $\delta f \approx 3.337$ KHz, providing the number $N \approx 1307$ of resolvable spots. The experiments included a Glan–Thompson linear polarizer and a four-prism beam expander, which operated with the light beam polarized in the plane of expansion and provided rather flat (nonuniformity ~11%) optical beam profile. During the experiments with the beam shaper, accurate angular adjusting of the incident light beam was achieved. This means that both the correct Bragg angle of incidence and the needed tilt angle were optimized. The 3 in achromatic doublet lens (#30-976, Edmund Optics) with the focal length of about 85 cm was used as the integrating lens, and the multi-pixel CCD-linear array consisting of 4.7 μm pixels was playing the role of a photo-detector. The layout of the optical scheme of the experiments is presented in Fig. 9.

B. Experimental Results

Experimental verification of the optical spectrum analysis under proposal was carried out with the Bragg cell, made of a unique calomel (α-Hg_2Cl_2) single crystal, which had an active optical aperture of about 52 × 2 mm; see Fig. 8. While operating at the optical wavelengths of 405 nm with a linear state of the incident light polarization oriented along the crystallographic axis [110] on the central acoustic frequency of about 71 MHz, this cell allowed a maximum input acoustic power of about 1.5 W.

The experiments consisted of two parts. The first part included measuring the bandwidth of the Bragg noncollinear two-phonon AOI. The second part of our experiments was related to estimating possible spectral resolution by involving this AOC into the optical spectrum analysis via measurements of the light intensity distributions specific to individual spots in the focal plane of the integrating lens for light deflected by that calomel AOC into the second order. Figure 10 shows the experimental plot for the frequency band shape inherent in the calomel cell. One can observe the characteristic variations of efficiency at the top of the experimental plot. The total

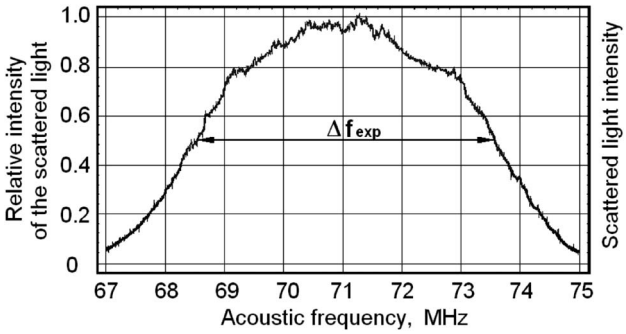

Fig. 10. Experimentally obtained frequency band shape for the AOC made of calomel. The full width at the half-maximum level can be estimated by about of $\Delta f_{\text{exp}} \approx 5.1$ MHz.

experimental frequency bandwidth at a –3 dB level has been estimated at $\Delta f_{\text{exp}} \approx 5.1$ MHz.

The calomel crystal is very effective, but a rather specific material whose transmission optical range is starting from 380 nm, while its main refractive indexes are high enough and equal about No = 2.083 and Ne = 3.038 at 405 nm. By this, it means that one can expect remarkable optical losses and reflections operating at 405 nm. Consequently, to optimize the experimental conditions, both the input and output facets of the calomel-made AOC should have anti-reflection coating. However, during our proof-of-principle experiments, the cell was not coated. This is why the diffraction efficiency was estimated in terms of the transmitted light, i.e., at the output facet of the calomel-made AOC. This means that the measured light intensity, transmitted through the cell without any input electronic signal at the piezoelectric transducer, was taken to be the unity. When the input signal is applied to the piezoelectric transducer, one can measure the portion of light intensity scattered into the second order and estimate its ratio to the initially measured transmitted light intensity. We consider this ratio, completely caused by an external signal, as the measure of the "diffraction efficiency." This experimentally obtained maximum ratio (i.e., the diffraction efficiency) at the optimal acoustic frequency of about 71 MHz was estimated by the value ~0.94 when the applied electronic signal power was about 1.2 W providing the acoustic power density ≤ 150 mW/mm^2.

Precise optical measurements were performed at the wavelength 405 nm to obtain sufficiently reliable estimations for the frequency resolution provided by the α-Hg_2Cl_2–cell, together with the above described optical system, including the CCD linear array. The realized measurement was done in the regime of the so-called "hot cell," i.e., with a radio-wave signal applied at the input port of the α-Hg_2Cl_2–cell. Figure 11 depicts the light intensity profile with the spot size of about 8.2 μm and the side lobe level of about 6.2%, which includes affecting the light distribution in a spot by the acoustic losses of 6 dB/aperture. This plot is a result of the standard computer processing realized by the CCD camera. The produced measurements showed that the main lobe of a partial optical beam gave the spot size lighting almost two pixels of the CCD row that provided a rather acceptable resolution of a pattern from the viewpoint of the sampling theorem.

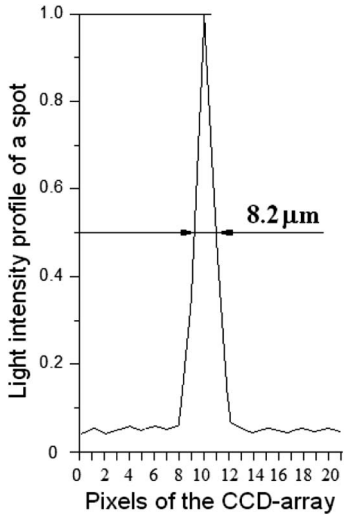

Fig. 11. Light intensity profile of an individual resolvable spot observed in the second order of scattering. It is the result of the standard processing provided by the CCD camera. The full width at the half-maximum of the main lobe can be estimated to be 8.2 μm.

As it has been noted, our experimental results have been obtained using the integrating lens with $F = 85$ cm at the wavelength 405 nm, so that, theoretically, the spot size is $d_S = \lambda F/D \approx 6.62$ μm. Together with this, the plot in Fig. 11 exhibits the experimental spot size $d_T = \lambda F/D_T \approx 8.2$ μm that corresponds to the aberration factor $\zeta_T \approx 1.2375$ (which includes, of course, optical imperfectness of the system), and, consequently, to the effective aperture $D_T \approx 4.202$ cm for the AOC. The last data show that about 20% of the active optical aperture of the AOC is lost because of the imperfectness of the lens and cell's material. Therefore, instead of a theoretical limit of the frequency resolution $\delta f = V/2D \approx 3.337$ kHz, one yields the measured value $\delta f_T = V/2D_T \approx 4.13$ kHz. Then, $\Delta\lambda_T = \Delta f_T \lambda/f_0 \approx 291$ Å (instead of the theoretical value $\Delta\lambda \approx 248.7$ Å) with $\delta\lambda_T = \lambda\delta f_T/f_0 \approx 0.235$ Å. Thus, the experimentally obtained number of resolvable spots is $N_T = \Delta f_T/\delta f_T = \Delta\lambda_T/\delta\lambda_T \approx 1235$ spots, which is rather close to the obtained theoretical estimation. Finally, the expected lighted length in the focal plane of the integrating lens is $L_{\text{CE}} = d_T N_T \approx 10.12$ mm, i.e., the capabilities of the experimental optical system lie in the frames of the exploited multi-pixel CCD-array.

The obtained results with calomel AOF (the spectral resolution $\delta\lambda \approx 0.235$ Å at 405 nm, which gives the resolving power $R \approx 17{,}200$) can be compared with, to the best of our knowledge, the most advanced acousto-optical spectrometers for space or airborne operations of the twenty-first century. For example, one can mention that an astrophysically oriented acousto-optical spectrophotometer, exploiting a TeO_2-based AOF, exhibited the spectral resolution $\delta\lambda \approx 12$ Å at $\lambda = 636.5$ nm [19], which is higher than the acousto-optical spectrometers used onboard space mission Mars Express with $\delta\lambda \approx 5$ Å at $\lambda \approx 1000$ nm [20] and space mission Venus Express with $\delta\lambda \approx 4.2$ Å at $\lambda \approx 650$ nm [21]. In addition, we can compare our results with the previously

mentioned KDP AOF, which exhibits a high spectral resolution $\delta\lambda \approx 0.625$ Å at $\lambda \approx 325$ nm giving the resolving power $R \approx 5,2005,200$ [5]. Together with this, one can take the other data from our introduction, which means that our results with calomel AOF can be considered like the best we can mention at the moment.

7. CONCLUSION

We have revealed novel physical aspects unique to square-law nonlinearity of the noncollinear two-phonon AOI governed by elastic waves of finite amplitude in birefringent crystals. This phenomenon manifests rather specific parametric nonlinearity within AOI, which can be observed at a reasonable level of acoustic power density in some anisotropic materials exhibiting moderate linear acoustic losses. First, strong nonlinear behavior of both the transmitted light intensity and the angular-frequency mismatch was distinguished. Then, these characteristics were studied theoretically. A sequence of the local unit-level maxima and a variety of the transfer function profiles specific to these maxima in the distribution of light scattered into the second order were identified and considered. As a result, the second unit-level maximum, providing one of the widest profiles for the transfer function, was selected. Potential application of this profile is related to a unique option for the precise spectrum analysis of optical signals. The criterion for similar selection was based on the above-mentioned combination of achieving already sufficiently wide transfer function and exploiting the unit-level maximum in the noncollinear two-phonon AOI distribution that requires power density that is not too high for manifesting the square-law nonlinearity. Then, we found, identified, and characterized an additional degree of freedom related to the noncollinear two-phonon AOI, which allows for the following possibility, i.e., namely, the two-phonon processes allow close to 100% efficiency with the fixed optical wavelength for various acoustic frequencies, as well as with the fixed acoustic frequency for various optical wavelengths because of the existence of an additional dispersive birefringence factor inherent in this phenomenon; see Fig. 5. Because the interplay between the scattered light waves and the incident ones is linear in behavior to the noncollinear two-phonon AOI in spite of strong acousto-optical nonlinearity peculiar, we have chosen to apply this effect to realize an advanced optical spectrum analysis with the doubled accuracy. By this, we mean that the second possibility, namely, the case with the fixed acoustic frequency for various optical wavelengths, was taken in a view of developing a new approach to the parallel spectrum analysis of optical signals. Moreover, because two-phonon processes give doubling of the spectral resolution in the acousto-optics, the spectrum analysis of optical signals with the significantly improved resolution has been obtained as well.

Usually, the spectral resolution of the collinear tunable AOF, for example, depends on the birefringence of the exploited crystal, which is fixed as a basic parameter of the chosen material. The approach under proposal makes it possible to replace that physically limited and the fixed birefringence of a crystal by the new relatively larger birefringence factor, inherent in square-law nonlinearity of the noncollinear two-phonon AOI. Moreover, this factor of birefringence can be varied through choosing the above described tilt angle whose acceptability depends on the symmetry of a crystal. In these circumstances, only the acoustic attenuation plays the role of a limiting factor, which restricts potential performances of spectrum analysis. In our case, a 6 dB level of the acoustical losses per optical aperture of the AOC was motivated and taken to avoid unnecessary strong limitations during the current stage of investigations.

To demonstrate the details of our analysis and to realize possible experiments, the crystals of tetragonal symmetry were considered as examples. Then, a very effective acousto-optical material, i.e., the calomel (α-Hg_2Cl_2) single crystal was selected as one of the best options for our goals. The needed theoretical, practical, and pre-experimental estimations were performed to design a really unique wide-aperture AOC based on the calomel crystal. The experiment was carried out at $\lambda = 405$ nm with a 5.2 cm aperture AOC made of calomel exited by the slow shear acoustic mode along the [110]-axis. Along with this, explored the use of rather specific directions for the optical waves to select adequate refractive indexes within the AOI. The results of the performed proof-of-principle experiments with this AOC, governed by elastic waves of finite amplitude, confirm in general the previously developed theoretical analysis and numerical estimations. Moreover, these results open the way to the application of the proposed innovative technique to an advanced optical spectrum analysis with the radically improved spectral resolution.

Funding. CONACyT (Consejo Nacional de Ciencia y Tecnología) (Project 61237).

Acknowledgment. The authors would like to thank Dr. William F. Wall (INAOE, Mexico) and Dr. A. Laskin (AdlOptica GmbH, Berlin, Germany) for the detailed discussion of this article and for their assistance within the preparation of our manuscript.

REFERENCES

1. N. Uchida and N. Niizeki, "Acoustooptic deflection materials and techniques," Proc. IEEE **61**, 1073–1092 (1973).
2. L. Wei, S. Yu-Nan, C. Fang, and B. Long, "Feasibility of non-collinear TeO2 acoustic-optic tunable filters used in the optical communication," Chin. Phys. Lett. **24**, 986–989 (2007).
3. Catalog of Acousto-Optic Tunable Filters-Free Space (Brimrose Corporation of America, Baltimore, MD, 2014).
4. C. Zhang, H. Wang, and Y. Qiu, "Study of the imaging performance for a noncollinear acousto-optic tunable filter," in *2010 Symposium on Photonics and Optoelectronics*, Chengdu, China, June 19, 2010, pp. 1–4.
5. N. S. Prasad, "Deep-UV based acousto-optic tunable filter for spectral sensing applications," Int. J. High Speed Electron. Syst. **17**, 857–866 (2007).
6. V. B. Voloshinov and N. Gupta, "Ultraviolet-visible imaging acousto-optic tunable filters in KDP," Appl. Opt. **43**, 3901 (2004).
7. N. Gupta, "Materials for imaging acousto-optic tunable filters," Proc. SPIE **9100**, 91000C (2014).
8. M. Gottlieb, A. P. Goutzoulis, and N. B. Singh, "Fabrication and characterization of mercurous chloride acoustooptic devices," Appl. Opt. **26**, 4681–4687 (1987).
9. N. Gupta, "Investigation of a mercurous chloride acousto-optic cell based on longitudinal acoustic mode," Appl. Opt. **48**, C151 (2009).

10. A. S. Shcherbakov, J. Maximov, and S. E. Balderas Mata, "Shaping the dissipative collinear three-wave coupled states in a two-mode medium with a square-law nonlinearity and linear non-optical losses," J. Opt. A **10**, 025001 (2008).
11. A. Korpel, *Acousto-Optics*, 2nd ed. (Marcel Dekker, 1997).
12. V. I. Balakshy, V. N. Parygin, and L. I. Chirkov, *Physical Principles of Acousto-Optics* (Radio I Svyaz, 1985).
13. M. P. Shaskolskaya, *Acoustic Crystals* (Nauka, 1982).
14. I. C. Chang, *Handbook of Optics*, M. Bass, ed., 2nd ed. (McGraw-Hill, 1994), Vol. **II**, Chap. 12.
15. J. F. Nye, *Physical Properties of Crystals: Their Representation by Tensors and Matrices* (Oxford University, 1985).
16. W. R. Klein and B. D. Cook, "Unified approach to ultrasonic light diffraction," IEEE Trans. Sonics Ultrason. **14**, 123–134 (1967).
17. J. W. Goodman, *Introduction to Fourier Optics*, 3rd ed. (Viva Books, 2007).
18. A. S. Shcherbakov, A. O. Arellanes, and S. A. Nemov, "Transmission function collinear acousto-optical interaction occurred by acoustic waves of finite amplitude," J. Opt. Soc. Am. B **30**, 3174–3183 (2013).
19. V. Y. Molchanov, V. M. Lyuty, V. F. Esipov, S. P. Anikin, O. Y. Makarov, and N. P. Solodovnikov, "An acousto-optical imaging spectrophotometer for astrophysical observations," Astron. Lett. **28**, 713–720 (2002).
20. O. Korablev, J.-L. Bertaux, A. Grigoriev, E. Dimarellis, Y. Kalinnikov, A. Rodin, C. Muller, and D. Fonteyn, "An AOTF-based spectrometer for the studies of Mars atmosphere for Mars Express mission," Adv. Space Res. **29**, 143–150 (2002).
21. O. Korablev, A. Fedorova, J. L. Bertaux, A. V. Stepanov, A. Kiselev, Y. K. Kalinnikov, A. Y. Titove, F. Montmessin, J. P. Dubois, E. Villard, V. Sarago, D. Belyaev, A. Reberac, and E. Neefs, "SPICAV IR acousto-optic spectrometer experiment on Venus Express," Planet. Space Sci. **65**, 38–57 (2012).